# Microscopic structure in syn- and anticlinic chiral phases of the antiferroelectric liquid crystal MHPOBC

F. Schmauder and A.Geiger [1]

Based on ab-initio derived potential parameters, classical molecular dynamics simulations of a MHPOBC (4-(**M**ethyl**h**eptyloxycarbonyl)-**p**henyl-4'-**o**ctyloxy**b**iphenyl-4-**c**arboxylat) two layer system were performed. Depending on boundary conditions and on temperature we obtain an orthogonal free standing film, as well as synclinic and anticlinic bulk structures. We compute layer spacings, analyse the layer structure and find reasonable agreement with experimental data. Molecular conformations in the gas phase, in the orthogonal phase and in the tilted phases are compared. We elucidate the influence of locale dipol moments on the clinicity of the phase. Polarisation profiles are calculated based on the molecular charge distribution and their contribution to the overall polarisation is discussed. The emerging picture is in close agreement with the so called $P_x$ model of tilted smectic phases.

[1]Physical Chemistry, University of Dortmund, Otto-Hahn-Str.6, D-44221 Dortmund, Germany

Phone: x-231-755 3937, Fax: x-231-755 3748, e-mail: alfons.geiger@udo.edu

# 1 Introduction

Despite increasing computing power simulations of mesophases on the basis of atomic-detail interaction models are still a challenge [1]. Whereas simulations of isotropic and nematic phases were performed largely on this level the smectic phase is mainly explored by simulations of simplified molecular models like hard sphero cylinders and Gay-Berne particles [2–8]. Experimental studies of smectic phases have determined a broad range of different properties; a few of them can be easily related to the molecular structure, for example the layer spacings in free standing films. For a more complete understanding, simulations in atomic detail are important [9–15]. In this work we study a prototype of the tilted chiral smectics which are candidates for high quality electro optic devices due to their ferroelectric and antiferroelectric behavior [16].

The existence of an antiferroelectric smectic phase ($SmC_A$) in liquid crystals (LC) shows that such an ordering can be stabilized in mesophases without long range positional order [17]. Before the discovery of the antiferroelectric structure it was believed that the packing effect as well as the Maier-Saupe-type interaction result in a uniform tilt in all layers [18]. After the discovery of the antiferro-electric properties of some compounds it became clear that tilted smectic phases can be either synclinic or anticlinic. The decisive features that control the stability of the different states are still not fully understood [16]. As in synclinic ferroelectric $SmC^*$, the tilt of the director in anticlinic antiferroelectric $SmC_A^*$ structures induces a spontaneous polarization perpendicular to the tilt plane in each layer. The primary feature of $SmC_A^*$ and $SmC_A$ is the emergence of the anti-clinic structure, independent of the chirality of the phase [19,20]. At present there are more than 1000 compounds which exhibit $SmC_A$ structures [21]. All these molecules are quite similar in their chemical structure and have large transverse dipole moments. The chemical structure and phase sequence of MHPOBC (4-

(**M**ethyl**h**eptyloxycarbonyl)-**p**henyl-4'-**o**ctyloxy**b**iphenyl-4-**c**arboxylat) is shown in Fig. 1. There is one oxygen linked alkyl chain like in 8CB and a hexyl chain contacted to the chiral center. The interplay between the two strong polar ester groups which reside in the core and close to the chiral center leads to a complex phase behavior.

MHPOBC has been studied extensivley as the first example of an antiferroelectric LC compound. Among these studies X-ray crystallography of a MHPOBC single crystal is particularly interesting, since it shows a characteristic conformational property [22]: The chiral chain is oriented nearly perpendicular to the core moiety. Further experimental studies indicate that this feature remains in the SmA as well as in the tilted phases, leading to an enhanced electrostatic interaction between neighboring layers [23–25] by reducing the interlayer distances between CO-groups.

The structural pecularities on the one hand and the large amount of experimental data available on MHPOBC, suggest classical molecualar dynamics simulation studies based on ab-initio derived potentials which realistically characterize the intramolecular flexibility and the charge distribution in MHPOBC. Although we are dealing in our simulations with chiral layers of R-enantiomers a helicoidal structure is suppressed by the geometry and the boundary conditions of the simulated systems. For similar reasons the subphases $SmC_\alpha$ and $SmC_\gamma$ can not occur in the simulations. Our simulations deal with free or periodic two layer structures, allowing orthogonal, syn- and anticlinic geometry without any helical pitch. They give insight into the smectic structure, molecular conformations and interactions in MHPOBC. Particularly we explore the syn- and anticlinic structures in detail and calculate orientational distributions of CO-groups in the tilted coordinate system.

The paper is organized as follows: The model force field for MHPOBC and the simulation technique are presented in Sec. 2 and 3. In Sec. 4 we characterize

the simulations for the orthogonal, syn- and anticlinic systems and discuss the molecular origin of the polar properties. In conclusion we summarize and discuss our results.

## 2  Force Field

Basic ingredients of a classical molecular dynamics simulation is a set of well defined interaction potentials, also called the force field. While force fields have been developed for several classes of substances it remains a demanding task to model inter- and intramolecular interactions of LC molecules with their subtle properties. Some widley used force fields fail in describing important soft modes like torsional degrees of freedom due to the lack of specifity [26, 27]. Also, many empirical and semi-empirical methods to obtain atomic partial charges are not able to reproduce the molecular dipole moment. Because of the important role of the electrostatic interactions and molecular flexibility, we parametrized the partial charge distributions and the torsion-potentials for MHPOBC from ab initio calculations, which we performed by Gaussian 94 [28] on a Hartree-Fock level using 6-31G* basis set (see also sec.2.1 and 2.2 )

As usual, atomic dispersion and repulsion interactions are described by Lennard-Jones potentials. For the interaction site we use a hybrid model: The core of MHPOBC is treated in atomic detail with explicit hydrogen atoms, the methyl and methylen groups in the alkyl tails are treated as one interaction site (united atom approach). Especially in the case of liquid alkanes it could be shown that experimental values of density and heat of vaporization could be reproduced well by the united atom approach. Such interaction parameters are used for all alkyl tails in our simulations [29]. The Lennard-Jones interaction parameters of all other sites, as well as the bond stretching and angle bending potentials were taken from

the OPLS parameter set of Jorgensen et al [30].

## 2.1 Torsion potentials

Torsion potentials arise in some force fields simply due to intramolecular 1,4-interactions (Lennard-Jones and Coulombic) across a torsion quadrupel [31]. In many cases it is necessary to add an additional dihedral angle potential:

$$U_{dih} = \sum_m^N k_m \left(1 + \cos(m\Psi_{\kappa\lambda\omega\tau} - \Psi_0)\right) \tag{1}$$

These potentials are specific to the molecular topology and in principle, all quadruples of four sites $\kappa\lambda\omega\tau$ in the molecule, which constitute a dihedral angle, have to be considered. Up to eight terms ($N = 8$) were necessary, subdivided into terms with $\Psi_0 = 0$ and $\Psi_0 = 90°$. We derive the parameters of $U_{dih}$ by fitting Eq (1) to energy values from the quantum mechanical ab-initio calculations: Choosing appropriate fragments of our target molecule, we perform geometry optimizations at fixed dihedral angles.

Fig. 1 shows all fragments and their derivatives which we study in more detail. Two fragments are chosen to mimic the core, two fragments catch the essential features of the achiral and chiral alkyl tails. The arrows indicate the dihedral angle, for which the torsion potentials have been determined explicitley. As an example, in Fig 2 we show the torsion potentials of some core fragments. (These correspond to the energy minimized structure with respect to all degree of freedom, except the torsion angle under consideration.) The potential barrier is highly influenced by the substituents and the extension of the resonant $\pi$-system. There are two very broad local minima. Like in many other cases the use of only non bonded intramolecular 1,4-interactions could not reproduce these ab-initio calculated potentials.

## 2.2 Electrostatic interactions

Partial Charges were obtained by a restrained electrostatic potential fit (RESP) applying the two stage procedure described in [32] to reproduce the ab-initio derived electrostatic molecular potential. It is well known that the Hartree-Fock approach overestimates the dipole moment by about 10%. This feature is used intentionally in this approach to mimic empirically polarisation interactions that are not considered explicitly in our model. To calculate the electrostatic potential for the RESP fit we chose points on several spheres of increasing radius ($\Delta r = 0.2 \, \text{Å}$) around each atomic site. The whole set of force field parameters is available via internet [33].

We calculated the electrostatic potential for a simplified derivative of MHPOBC where a methyl group substitutes the $C_8H_{17}$ tail and an ethyl group the $C_6H_{13}$ tail. Consequently the force centers in these tails of MHPOBC are treated without partial charges in the simulation. Because we used only the minimum energy conformation for the ESP calculation we examined whether the molecular dipole moment in other torsion states can be reproduced by the same partial charges. The dipol moment of the fragment molecule of Fig. 3 has been calculated in two different ways: (a) ab-initio at fixed torsion angles for the structure, which has been energy minimized with respect to the other degrees of freedom, (b) from the partial charges and energy minimized structure of the force field. In the regions of the flat energy minima, which corresponds to the conformations of heighest probability, the fixed charges of the force field reproduce the ab-initio values within 10%.

We also calculated for the full MHPOBC molecule the molecular dipole moment in different torsion states: Fig. 4 reveals an angular symmetry of the dipole moment which substantially differs from the fragment molecule of Fig. 3. There is a comparable probability for a conformation of MHPOBC with a very high and a very low dipole moment. This strongly different behavior can be explained mainly

6

by the presence of the free OH-group and the lack of the ether oxygen in the fragment. In the MHPOBC molecule the extrema are produced by roughly parallel and antiparallel orientations of the CO-groups. However, the maximum value of the dipole moment can not be explained simply by the sum of the two ester groups $(-O = CO-)$: We find for both groups a local dipole moment of approximately $1.7\,D$ which would lead to a maximum value of $3.4\,D$ that is much lower than the maximum in fig. 4. This indicates an obvious difficulty to describe mesogens by a few localized dipoles.

# 3 Simulation outline

All simulations are performed with the program MOSCITO [34]. For the nonbonded Lennard-Jones interactions the minimum image convention and a cut-off radius of $0.9\,nm$ were used. Electrostatic interactions are treated by the Particle Mesh Ewald summation method [35] with a grid width of $1\,\text{Å}$. The equations of motion are solved via the leap-frog algorithm with a time step of $2\,fs$. To maintain NPT conditions in all simulations we used the Berendsen coupling method [36] with coupling constants for temperatures and pressure $\tau_T = 2ps$ and $\tau_p = 10ps$ (when using a roughly estimated isothermal compressibilty of $0.5 \cdot 10^{-3}MPa^{-1}$). The lengths of the simulation runs, including the equilibration period, extended from $8$ to $37.5\,ns$ (Tab. 1). The averages presented below were then computed from the last part of the trajectory (at least $2.5\,ns$), when the tilt reached a steady state.

The starting configurations of the systems were constructed as follows: Each molecule was assigned to a rectangular cell of $0.5 \times 0.5 \times 3.7\,nm^3$ roughly according to the shape of the molecule. A stretched conformation of the molecule was used. Successive molecules were arranged antiparallel to minimize the dipole moment of the complete system and to preserve a $C_2$ symmetry of the system. The total

simulation box was build up from six rectangular cells in x- and y-direction and two cells in z-direction (two layers of 36 molecules each). No molecular tilt and no molecular bent were present in the starting configuration.

We have simulated a free standing film as well as three bulk liquid crystal structures. In Tab. 1 the average box dimensions and densities $\rho$ of the bulk systems after equilibration in the NPT ensemble are given. To create and treat a free standing film system, using the particle mesh Ewald summation method for the electrostatic interactions, as implemented in MOSCITO [34], we used the following approach: The simulation box of the bulk systems is expanded in z-direction (the layer normal) to 8 nm and the scaling of the box length by the Berendsen barostat is switched off in this direction. Thus in the simulation, a system is reached, which is still periodic in all three cartesian directions (to use the Ewald summation), but the films of two molecular layers are separated in the periodic system by a gap of 8 nm, reducing the interactions between them to a minimum.

In the free standing film simulation (labeled FSF) at 375 K the smectic order remains and practically no tilt appears (Fig. 5; a more detailed discussion is following). From this film structure, a bulk system is constructed by applying box scaling, which reduces the box size in z-direction and brings the films in contact. This produces a periodic bulk system without gaps. From this systemwe start two equilibrium runs with different temperatures. In the following the resulting systems are called SmX(375K) and SmC$_A$(400K) for reasons, which become evident later. From the latter one we finally obtain a system, labeled SmC$_A$(375K), by cooling back to 375 K and equilibrating again. Obviously, one of the two systems SmX(375K) and SmC$_A$(375K) must be metastable. It shoud be noted here, that in the SmX-Simulation run, after 7ns, when the molecules started to tilt, this process was supported, by setting the thermostat for 10ps on ah higher temperature. This results in the dip of the density in Fig. 6.

# 4 Results

## 4.1 Simulation runs

Fig. 6 and Fig. 7 show the development of density, tilt angles, azimuth angles and order parameter of these bulk simulations. Simulation $SmC_A(375K)$ is not shown explicitley. The definitions of tilt, azimuth and order parameter are strongly related to each other: First we define the elements of a tensor $\mathbf{Q}$ which describes the orientational order within a single layer:

$$Q_{\alpha\beta} = \frac{1}{2N} \sum^{N} \left( 3u_\alpha^j u_\beta^j - \delta_{\alpha\beta} \right) \tag{2}$$

$u_{\alpha,\beta}^j$ are the components of the unit vector representing the orientation of the core of molecule $j$ (the vector between the center of mass of the outer phenyl rings of the core) and $\alpha, \beta = x, y, z$. We sum over all N molecules within one layer. The largest eigenvalue of the orientational order tensor represents the orientational order parameter $S$ and the corresponding eigenvector the director $\mathbf{n}$ of this layer. The optical tilt angle $\theta$ is defined as the angle between the director (as defined above) and the layer normal. The tilt direction of the layer is given by the projection of the director onto the layer plane, the so called c-director. Consequently we obtain the azimuth as the angle between the c-director and a laboratory fixed axis. The difference of the azimuth angles of two neighboring layers describes the clinicity of our simulated systems. In addition to the optical tilt, given by the orientation of the director, we have also calculated the so called X-ray tilt that is often smaller (Zig-zag model [37]). In the simulation we obtain the X-ray tilt from the layer spacing in the tilted ($d$) and non tilted ($d_0$) state (for the determination of $d_0$ see chapter 4.2):

$$\cos(\theta) = \frac{d}{d_0} \tag{3}$$

From Fig. 5 to Fig. 7 we can see the following general behavior: Whereas density and order parameter reach a steady state very quickly this is not the case for tilt and azimuth. The behavior of the angles in Fig. 6 show clearly that simulation SmX (at 375 K) ends up in a synclinic geometry (after about 15ns both azimuthal angles are close to $\pm180°$) whereas simulation $SmC_A$ at 400 K ends up in an anticlinic geometry (in Fig. 7b after about 5ns the azimuthal angles are close to 0° and $\pm180°$), although both runs start from the same configuration (the end point of the FSF simulation, Fig. 5, as explained above). Fig.8 gives a snapshot of both systems (the pictures comprise several periodicaly repeated simulation boxes). It is interesting to realize that the simulation SmX (Fig.6) remains in the orthogonal symmetry of the FSF simulation during the first 5ns. At the density dip after 7 ns we supported the beginning tilt process by a short 10 ps temperature pulse. The order parameter in the individual layers is always very high between 0.95 and 0.98. The tilt behavior of our FSF-simulation shows some subtle detail: Due to the small deviation of the tilt from zero in each layer (Fig. 5a), we categorize this system as orthogonal. But because of the non vanishing tilt we can also observe a well defined anticlinic geometry (azimuth angles of $\pm90°$, Fig. 5b). In the bulk simulations the tilt is more pronounced (Fig. 6 to 7). Comparing optical and X-ray tilt, in the $SmC_A$ phase at 400K we find that the optical tilt is slightly higher whereas in the synclinic geometry of SmX no difference can be observed. Lowering the temperature (simulation $SmC_A$ at 375 K) leads to a decrease of the tilt and the difference between optical and X-ray tilt observed at 400 K disappears.

## 4.2 Layer spacing

Due to rather strong variations of the tilt angle the layer spacing $d$ is also strongly fluctuating. Simulation FSF(375K) produces in good approximation orthogonal symmetry. Therefore we try to determine the layer spacing $d_0$ from this state by

calculating the center of mass profile (Fig. 9), fitting a Gaussian to each layer and measuring the distance of the maxima. We obtain 3.90 nm for the FSF simulation. Concerning the bulk, we extract a value for $d_0$ from the simulation SmX by an extrapolation of the linear correlation Eq.(3) between the cosine of the optical tilt angle and the layer spacing: We take the first 12 ns of our simulation (Fig. 6) and plot at each time step $d$ (in this case half the box length in z-direction) versus $\cos(\theta)$. We find $d_0 = 3.74$ nm for the bulk phase from the extrapolation of the linear regression line to $\cos\theta = 1$. This may be compared with the experimental value $d_0 = 3.52$ nm for the non tilted SmA Phase. The higher spacing in the FSF reflects the reduced interaction in the two layer film compared to the bulk.

A comparison of the layer spacing $d$ from Tab. 1 (half the box length in z-direction) in the tilted states allows us further classification of our simulations. Experimentally, the liquid crystal transforms at low temperatures into the anti-clinic state with a layer spacing of 3.39 nm. We find a rather compatible value of 3.44 nm in the similarly structured simulation $SmC_A$ at 400 K. This value slightly increases when the temperature is decreased ($SmC_A$ at 375 K). This increase is mainly due to a smaller tilt. The synclinic simulation SmX shows a rather small layer spacing, indicating that this simulation resembles more one of the metastable crystalline phases observed in [22] where the spacing is quite low (3.21 nm). Several properties of this system, which will be discussed later, also indicate a more solid like behavior. As observed for the anticlinic states, a continuation of this simulation at a higher temperature (400K, not discussed further here) reveals a decrease of the layer spacing.

## 4.3 Center of mass and density distributions

To elucidate the structure of the smectic layers in more detail we computed center of mass distributions $f(z)$ and density profiles $\rho(z)$ along the layer normal $z$. In

Fig. 9 one can clearly observe a layered structure. Due to our limited observation time in all three cases, the profiles of the two constituting layers are not identical as they should. But clearly, the distribution of the molecular centers within the layers shows some structure. Due to the solid glass like properties mentioned above, the simulation SmX shows the sharpest peaks. Before discussing the internal structure of the layers in more detail, we make some comparisons with experimental order parameters of the smectic mass distribution. Unlike in the case of e.g. 8CB, which has an alkoxy group of the same length, the center of mass profile is not sinusoidal [11, 38] but can be expanded according to the McMillan theory:

$$f(z) = \rho_0 \left[ 1 + \sum_{l=1}^{\infty} 2\tau_l \cos \left( \frac{2\pi l}{d} z \right) \right] \tag{4}$$

$$\tau_l = \left\langle \cos \left( \frac{2\pi l}{d} z \right) \right\rangle = \int_0^d f(z) \cos \left( \frac{2\pi l}{d} z \right) \mathrm{d}z \tag{5}$$

Here, the $\tau_l$ are smectic order parameters. In [38] the authors extract both, width and smectic order parameters, from higher order Bragg peaks. In our simulations we can get these values independently. In all studied systems they do not vary very much, but this is also true for the experimental values [38]. The magnitudes of $\tau_l$ are in very good agreement: The values 0,75, 0,28 and -0.03 for $SmC_A$ at 375K from Tab. 1 have to be compared with the experimental values 0.72, 0.27 and 0.04 from the anticlinic phase in [38]. The experimentally determined reduced layer widths $\sqrt{<z^2>}/d$ in the anticlinic phase are in the range 0.12-0.14. These values are reproduced in our simulations $SmC_A$ and FSF which have liquid crystal character (Tab. 1). In line with the reduced mobility and higher order in the SmX-phase we find there the lowest value 0.11.

All center of mass distributions show roughly a three peak structure. To understand this feature we calculated the center of mass distribution separately for molecules pointing in $+z$ and $-z$ direction. As seen from Fig. 9 these distributions are asymmetric: Beyond a certain point the molecule does not permeate further

into the layer, leading to an edge in the distribution. The observed features reveal a partial bilayer structure of each single layer. The origin of this behavior has to be searched in a special overlap of the molecules.

To describe this overlap in more detail we calculated mass density profiles $\rho(z)$ for different parts of the molecule: We choose the biphenyl groups, the chiral and the achiral tail according to Fig. 1a. Additionally we plot the full density of the simulations FSF and SmC$_A$ (Fig. 10). As in the center of mass distribution the overall mass profile is not purely sinusoidal. Discriminating between the two possible orientations of the molecules, Fig. 10, shows a well defined arrangement:

The dominating feature is *the perfect overlap of the biphenyl* groups. This leads to an interlayer contact which is mainly established by the (strongly bent) chiral tails, as can be seen from the strong overlap of the distributions from oppositely oriented molecules in the interlayer space at 3 to 4 nmin Fig.10 (lower distributions in Figs. 10a,b).

## 4.4 Contributions of molecular fragments to layer thickness

As shown by Jang et al. [12], depending on the average orientation , the contribution of different parts of the MHPOBC molecules to the overall layer thickness can be very different. The authors computed projections of molecular segment vectors to the layer normal to define sublayer spacings. They showed that the chiral tail is more tilted than the achiral tail. The question arises, whether this behavior is a consequence of the condensed phase or a property of the single molecule itself. In the following we use projections of tail vectors to the core axis vector of MHPOBC molecules to characterize the molecular conformations. To reveal the role of the single molecular conformation we compute also distributions from a simulation of a single molecule in the gas phase at 375K and compare these results with the molecules in our bulk and FSF simulations. Core and tails are defined as given in

Fig. 1a. The core vector connects the outer carbon atoms of the core phenyl rings, the tail vectors extend from the oxygen (achiral tail) or from the chiral center to the terminal methyl carbons in each tail. First we discuss the distribution of the end-to-end distance of the achiral tail (bottom of Fig. 11b). We find two maxima, each one resulting from a certain trans/gauche ratio within the chain. The stretched (all trans) conformation dominates only in the FSF simulation, as seen from the peak at 1.0 nm, which is the fully extended chain length. In the $SmC_A$ simulation and even more in the gas phase a slightly more compact conformation dominates. If we compute the length of the projections of the tail vectors to the molecular core axis (upper part of Fig. 11b) the distributions show a maximum and a shoulder, which are only slightly shifted from the peak positions of the end-to-end distributions. This reflects a preference for a non-bent linear conformation of the achiral tail. Only in the gas phase there is a very broad distribution with a shifted maximum indicating stronger bents.

The chiral tail shows a more complex behavior. In each simulated phase we find in the end-to-end distribution a peak at 0.87 nm which corresponds to the fully extended, all trans conformation. This conformation dominates in the FSF and in the gas simulation. In the gas phase we find a third maximum belonging to a compact conformation. The distributions of the projections are very broad and extend down to zero indicating a frequent strong bent of the chiral tail. How this influences the interaction between CO groups is discussed later. The fact that in the gas phase compact and bent conformations are much more frequent than in the bulk reflects the importance of packing effects for the molecular conformation in the condensed phases. The clear preference for a stretched conformation of both tails in the FSF correlates with the enlarged layer thickness of this structure.

14

## 4.5 Mutual orientation of lateral carbonyl groups

Here we consider the so called lateral carbonyl group, i.e. the one which is close to the chiral center. To analyze the intermolecular interaction between these groups we calculated positional and orientational correlation functions, separating inter-layer and intralayer contributions. We consider the pair correlation function $g(r)$ and the orientational correlations function $g_1(r)$:

$$g^{CO}(r) = \frac{1}{\rho N} < \sum_{i \neq j} \delta(r - |\mathbf{r}_{ij}^{CO}|) > \tag{6}$$

$$g_1^{CO}(r) = \frac{1}{\rho N g^{CO}(r)} < \sum_{i \neq j} P_1(\mathbf{u}_i^{CO} \cdot \mathbf{u}_j^{CO}) \delta(r - |\mathbf{r}_{ij}^{CO}|) > \tag{7}$$

$\mathbf{r}_{ij}^{CO} = \mathbf{r}_i^{CO} - \mathbf{r}_j^{CO}$. $\mathbf{r}_i^{CO}$ is the position of the carbonyl carbon of molecule $i$, $\mathbf{u}_i^{CO}$ is the unit vector directed along the carbonyl bond and $P_1(\cos x)$ the first Legendre polynomial. The sums may be extended over different categories: pairs in the same and in different layers (intra and inter), or pairs with arbitrary orientation or with parallel/antiparallel orientation of the molecular axis. All pair correlation functions are summed over all such pairs with $|\mathbf{r}_{ij}^{CO}| = r$.

The orientational correlation between the lateral CO groups in the same layer and belonging to molecules of the same core axis orientation (intra sublayer: dashed lines in Fig. 12) are positive and strongly structured up to large separations in both simulations. The positive sign reflects a sublayer structure of parallelly oriented carbonyl groups. Note that the lateral carbonyl groups are "diluted" by achiral alkyl tails stemming from molecules which show in the opposite direction. This strong overlap and the sublayer formation can be seen clearly by comparing the density profiles for the lateral CO groups (Fig. 14b) and for the achiral tails (Fig. 10).

The interlayer orientational distribution functions (full lines in Fig. 12) are calculated for pairs of molecules having opposite orientations of their molecular core

15

axis and being in different layers. For the interlayer orientational correlations we find that clinicity strongly changes the mutual lateral carbonyl group orientation: whereas in the synclinic simulation the carbonyl groups in different layers are correlated antiparallely, we observe a change in sign in the anticlinic simulation.

It has to be noted that the interlayer radial pair distribution functions $g^{CO}(r)$ of the considered CO groups show broad maxima beyond 1nm. Therefore the interlayer orientational correlations $g_1^{CO}(r)$ at such distances are most important. Moreover, selecting molecules with parallel core orientation for the shown intra layer orientational distributions and antiparallel pairs for the inter-layer orientational distributions singles out contributions from the same sublayer respectively the adjacent sublayer of the neighbouring layer. In summary, the discussed distributions show clearly that each layer is made up of two sublayers with preferential parallel mutual orientation of the lateral CO groups within the sublayers. In adjacent sublayers of neighbouring layers the lateral CO groups are orientated antiparallely in the synclinic and parallely in the anticlinic phases, in accord with the schematic representation of Fig.16.

## 4.6 Polarisation and Polarity profiles

In this section we first calculate the electrostatic polarisation of each layer. In a second step we analyse the contributions of the different CO groups to the polarisation.

For symmetry reasons the spontaneous polarisation must be directed perpendicular to the tilt plane, that means parallel to *the tilt plane* normal $\mathbf{y}$, which is determined by the layer normal $\mathbf{z}$ and the director $\mathbf{n}$ within a layer (as introduced in the previous section 2.1). To calculate the polarisation $P_s$ of a given layer we sum over all N molecular dipole moments $\boldsymbol{\mu}_i$ within the layer (calculated from the partial charge distribution of the molecules) and project the resulting vector to the

tilt plane normal $\mathbf{y}$ (in fact the simulations yield the result, that the component perpendicular to $\mathbf{y}$ is numerically close to zero):

$$P_s = \mathbf{y} \sum_i^N \boldsymbol{\mu}_i \quad \text{with} \quad \mathbf{y} = \frac{\mathbf{z} \times \mathbf{n}}{|\mathbf{z} \times \mathbf{n}|} \tag{8}$$

As can be seen from eq.8 the tilt direction and the sign of $P_s$ are unambiguously interrelated.

Here we focus on simulation $\mathrm{SmC_A}(375\mathrm{K})$. We have calculated $P_s$ for each layer separately. Our simulation develops a pronounced polarisation $P_s \neq 0$ after about $15\,\mathrm{ns}$ when the tilt increases (Figs. 13). If we take the second half of our simulation we find an average $P_s$ of $(-90 \pm 10)\,\frac{\mathrm{nC}}{\mathrm{cm}^2}$ and $(-56 \pm 10)\,\frac{\mathrm{nC}}{\mathrm{cm}^2}$ for the two layers. The discrepancies between these two values indicate, that our simulation did not yet reach full equilibrium. Nevertheless the average value is in good agreement with the experimental value that bears out to be $-70\,\frac{\mathrm{nC}}{\mathrm{cm}^2}$ [39]. The sign of $P_s$ deserves an additional comment: Due to the fact that we calculate $P_s$ in each layer separately we obtain the same sign in each layer. Because the tilt alternates, the direction of the spontaneous polarisation vector alternates in our simulation as well (antiferroelectric structure). The sign itself is in accordance with the chirality of our simulated phase (R-MHPOBC).

In the following we concentrate again on the carbonyl groups as the locus of the most important local dipole moments and compute their orientational distribution with respect to a coordinate system defined by the molecular tilt. As explained above, in tilted phases the director $\mathbf{n}$ of a layer and the layer normal $\mathbf{z}$ span the so called tilt plane and the tilt plane normal $\mathbf{y}$ describes the orientation of the spontaneous polarisation. To localize the origin of the spontaneous polarization $P_s$ we compute profiles $< \mathbf{u}_i \cdot \mathbf{y} >_z$ along the layer normal $\mathbf{z}$, where $\mathbf{u}_i$ is a unit vector along one of the CO groups and $\mathbf{u}_i \cdot \mathbf{y}$ its projection along the tilt plane normale $\mathbf{y}$. The resulting z-dependence of this projection for the the *core* CO groups in $\mathrm{SmC_A}$ is shown in Fig. 14a. It is all over negative in accordance with the

value of $P_s$ already calculated. But it has to be kept in mind that the direction of $\mathbf{y}$ alternates between the layers due to the alternating tilt. The net polarisation is localized in the region of the maxima of the center of mass distribution as indicated in the figure and is roughly of same size in each layer. In contrast, the polarisation profile of the *lateral* CO groups (Fig. 14b) is different in the two layers: The integral, which represents the contribution of the lateral CO group to the spontaneous polarisation $P_s$ is close to zero in each layer, due to pronounced cancellation effects.

From Fig. 14b it seems that layer 1 (0 to $3,5\,\mathrm{nm}$) is better equilibrated because the profile is more symmetric to the minimum of the number density distribution of the layer. Interestingly, this number density does not reach zero between the two layers, i.e. the lateral CO groups from different layers may slightly overlap.

To clarify the role of the lateral CO-groups we also calculate the $z$ dependent orientational profile $< \mathbf{u}_i \cdot \mathbf{x} >_z$, the integral of which determines the polarisation $P_x$ ($\mathbf{x}$ is perpendicular to $\vec{y}$ and located at the intersection of the tilt plane and the layer plane, thus pointing within the smectic layer in the tilt direction.). The polarization $P_x$ at the layer boundaries plays an important role in models of antiferroelectrics [21, 40] but does not contribute to the macroscopic spontaneous polarisation $P_s$. According to these ideas, a close approach (due to the bent shape of MHPOBC) and strong interaction of local dipole moments across the interlayer boundaries, established by the polarisation $P_x$, could yield a decisive contribution to the stability of the anticlinic structures, otherwise packing effects would lead to the synclinic geometry.

Fig. 15a shows the normalized $P_x$-profile $< \mathbf{u}_i \cdot \mathbf{x} >_z$ for the lateral CO groups, the interlayer boundaries being localized at 0, 3.5 and 7nm (with periodic repetitions). Because the calculation of $< \mathbf{u}_i \cdot \mathbf{x} >$ is based on individual layers, the profile has to be interpreted with care in the case of the anticlinic geometry. To refer to

18

the same (laboratory fixed) direction in the tilt plane of the adjacent anticlinic layers and to get the correct sign of the z-profile of $P_x$ we had to reverse the sign in one half of the distribution 15a. Fig. 15b shows the same distribution for the synclinic structure of SmX(375K). Due to the more ordered character, here the density distribution of the lateral CO groups is more peaked and more pronounced zero between the maxima.

Comparing the orientational distributions of Figs. 15a and b for the anticlinic and synclinic structures and keeping in mind its periodic repetition in z-direction, a clear picture emerges, which is in perfect agreement with the so called $P_x$-model for the herringbone structure of tilted smectic liquid crystals (when the tilt plane in adjacent smectic layers are parallel to each other) [21]: Each layer is built up of two sublayers with antiparallel orientation of their $P_x$-polarisation. The difference between the syn- and anticlinic structures being the mutual orientation of adjacent sublayers across the layer boundaries which are antiparallel in the syn- and parallel in the anticlinic structure. This is depicted schematically in Fig.16 which has been adopted from [21]. It should be noticed that the $< \boldsymbol{\mu}_i \cdot \mathbf{x} >_z$ distribution is also in agreement with the interlayer orientational correlations discussed in section 4.5 (Fig. 12).

In the distributions of Fig. 15 a small detail deviates from the global picture of Fig.16: At the edge of the sublayer small sheets of opposite polarisation appear which may approach each other very closely, especially in the case of the anticlinic structure. While keeping the overall symmetry, they may play an important role for the electrostatic interlayer interactions, to 'glue' together the otherwise parallel orientation of the adjacent sublayers in the $SmC_A$ structure. In SmX the sublayers are more separated (as the number density distribution shows) and thus this effect vanishes.

# 5 Summary and Conclusions

The initial step of this study is a careful construction of the intra- and inter-molecular interaction potentials from quantum mechanical ab initio calculations. In our MD simulations the bulk systems spontaneously form syn- and anticlinic tilted layer structures. Whereas a free standing double layer film shows a more orthogonal orientational order.

Although we start our simulations from linear, elongated molecular conformations, the molecules bent and reproduce closely the experimentally observed layer thickness, as well as a mass distribution within the layers which is in accordance with the experimentally determined smectic McMillan order parameters.

The dominating feature of the density distribution within the layers is the perfect overlap of the rigid biphenyl cores of all molecules, independent of their orientation. In conjunction with the bent tail conformation this determines the layer thickness with the non-chiral tail being less stretched and less bent than the chiral tail. The two flexible tails constitute a pronounced layer substructure, with a major overlap between the chiral chains of neighbouring layers. This leads to a close inter-layer approach and interaction between the lateral carbonyl groups.

The orientational correlation functions in conjunction with the mass density profiles show that each layer is made up of two sublayers with preferential parallel mutual orientation of the lateral CO groups within the sublayers. In adjacent sublayers at the layer boundaries the lateral CO groups are oriented antiparallel in the synclinic and parallel in the anticlinic phases (Fig.16).

It is interesting to note that the antiparallel lateral CO orientation in adjacent sublayers of the synclinic structure is accompanied by a more pronounced gap in the density profiles of these groups, whereas a slight overlap of these sublayers in the anticlinic structure (Fig.15) causes a parallel orientation in both sublayers, comparable to the uniform alignment within a single sublayer. Concerning the

orientation of the lateral CO groups with respect to the tilt plane (which is defined by collective or individual molecular tilts) we observe in agreement with IR studies a more "in plane" orientation in the anticlinic geometry which changes to a "more upright" orientation in synclinic geometries at higher temperatures [41].

The spontaneous polarisation which our simulation reveals for the anticlinic structure $SmC_A(375K)$ is in perfect agreement with the structural ideas developed for antiferroelectric smectic liquid crystals: according to the symmetry, $P_s$ is pointing perpendicular to the tilt plane with opposite sign in adjacent layers, in accord with the alternating tilt. Also the magnitude of the average spontaneous polarisation is in close agreement with the experimental results. In contrast, the spontaneous polarisation in the two layers of the synclinic $SmX(375K)$ structure shows strong fluctuations during the whole simulation run of 25ns. Obviously, the periodic boundary conditions of our system do not allow the formation of a stable ferroelectric polarisation pattern.

The role of the core CO group is clearly to establish in each layer the observed net polarisation normal to the tilt plane, thus developing the antiferroelectric character of the $SmC_A$ structure. On the other hand, the contribution of the lateral CO groups to this normal polarisation cancels out largely within each layer. The important role of these lateral groups is in the development of a net polarisation $P_x$ in the direction of the tilt plane in the antiferroelectric structure $SmC_A$. The prominent feature of the anticlinic structure is the antiparallel orientation of the $P_x$ polarisation in the two sublayers of each layer, established by the parallel orientation of the lateral CO groups in adjacent layer boundaries. In the synclinic SmX structures no $P_x$ polarisation emerges due to antiparallel orientation of the lateral CO groups in neighbouring sublayers. This finding perfectly agrees with the so called $P_x$ model of the tilted smectic phases of [21] as depicted in Fig.16

The electrostatic stability of the syn- and anticlinic structures afford antiparallel

orientation of neighbouring layer polarities. Thus in the anticlinic structure the overlapping density distributions suggest one common "boundary" layer which acts as a "glue" between the two more interior layers. In the synclinic case the density distribution shows strongly decoupled layer boundaries which have to be polarised oppositely to provide low energies. The transition from an anti- to a synclinic structure can be explained by the fact that an increased temperature reduces the overlap between adjacent layers which then favors an antiparallel orientation of the lateral (chiral) CO groups.

Although our results suggest that the dipolar interactions at least contribute to the observed structural changes, our simulations can not answer definitively the question whether the dipolar interactions in the system are their cause or result. An answer to this question may be given by a simulation study in the spirit of a model experiment with a systematic variation of the dipolar strength. Also, the simulation of larger systems with more than two layers (as free standing film and bulk liquid) will be needed. Beyond the present study on the basis of periodic two layer systems, the structural details can be generalized to more sophisticated models of antiferroelectric liquid crystals [42]. Acknowledgement:

# References

[1] M.R. Wilson, 1998. *Molecular Modelling, In: Handbook of Liquid Crystals, Fundamentals, Theory of the Liquid Crystaline State*, volume 3B edited by . D. Demus, J. Goodby, G.W. Gray, H-W. Spiess, and V. Vill, Wiley VCH, pp. 72–86.

[2] A. Stroobants, H.N.W. Lekkerkerker, and D. Frenkel. Evidence for one-, two- and three dimensional order in a system of hard parallel spherocylinders, 1987. Phys. Rev. A, 36:2929–2945.

[3] I.M. Withers, C.M. Care, and D.J. Cleaver. A computer simulation study of tilted smectic mesophases, 2000. J. Chem. Phys., 113:5078–5090.

[4] G.R. Luckhurst and G. Saielli. Computer simulation studies of anisotropic systems. XXXII. Field-induction of a smectic a phase in a Gay-Berne mesogen, 2000. J. Chem. Phys., 112:4342–4350.

[5] M.A. Bates and G.R. Luckhurst. Computer simulation studies of anisotropic systems. XXX. The phase behavior and structure of a Gay-Berne mesogen, 1999. J. Chem. Phys., 110:7087–7108.

[6] P.J. Camp, M.P. Allen, and A. Masters. Theory and computer simulation of bent-core molecules, 1999. J. Chem. Phys., 111:9871–9881.

[7] M. Mazars, D. Levesques, and J.J. Weis. Monte Carlo study of a semiflexible liquid crystal model: The smectic phase, 1997. J. Chem. Phys., 106:6107–6115.

[8] S.C. McGrother, A. Gil-Villegas, and G. Jackson. The effect of dipolar interactions on the liquid crystalline phase transitions of hard spherocylinders with central longitudinal dipoles, 1998. Mol.Phys., 95(3):657–673.

[9] M.A. Glaser, R. Malzbender, N.A. Clark, and D.M. Walba. Atomic–detail simulation studies of smectic liquid crystals, 1995. Molecular Simulation, 14:343–360.

[10] M.A. Glaser, R. Malzbender, N.A. Clark, and D.M. Walba. Atomic detail simulation studies of tilted smectics, 1994. J.Phys.:Condens. Matter, 6:A261–A268.

[11] Y. Lansac, M.A. Glaser, and N.A. Clark. Microscopic structure and dynamics of a partial bilayer smectic liquid crystal, 2001. Phys.Rev.E, 64.

[12] W.G. Jang, M.A. Glaser, C.S. Park, K.H. Kim, Y. Lansac, and N.A. Clark. Evidence from infrared dichroism, x-ray diffraction, and atomistic computer simulation for a "'zig-zag"' molecular shape in tilted smectic liquid crystal phases, 2001. Phys.Rev.E, 64:1–12.

[13] H. Toriumi, Mikami M. Takeuchi M. Yoshida, M., and Mochizuki.A. Computer simulation of an antiferroelectric liquid crystalline molecule: The origin of bent structure formation and the molecular packing property of MHPOBC in crystalline phase, 1996. J. Phys. Chem., 100:15207–15210.

[14] M. Yoshida, N. Seo, K. Hori, and H. Toriumi. Computer simulation of biphenyl-phenyl ester liquid crystals, 2001. Mol. Cryst. Liq. Cryst., 365:813–826.

[15] H. Toriumi, M. Yoshida, N. Kamiya, and M. Takeuchi. Molecular dynamics simulation of an antiferroelectric liquid crystalline molecule MHPOBC: Conformational transitions in smectic phases, 2003. Mol. Cryst. Liq. Cryst., 402:31–42.

[16] S.T. Lagerwall. *Ferroelectric and Antiferroelectric Liquid Crystals.* Wiley-VCH, 1999.

[17] A.D.L. Chandani, E. Gorecka, Y. Ouchi, H. Takezoe, and A. Fukuda. Antiferroelectric chiral smectic phases responsible for the tristable switching in MHPOBC, 1989. Jpn.J.Appl.Phys., 28:L1265–L1268.

[18] P.G. DeGennes and J. Prost. *The Physics of Liquid Crystals*. Oxford Science Press, 1993.

[19] I. Nishiyama and J.W. Goodby. A non-chiral swallow-tailed liquid crystal exhibiting a smectic C phase that has an antiferroelectric structure, 1992. J. Mater. Chem., 2:1015–1023.

[20] A. Fukuda, Y. Takanishi, T Isozaki, K. Ishikawa, K. Ishikawa, and H. Takezoe. Antiferroelectric chiral smectic liquid crystals, 1994. J. Mater. Chem., 4:997–1016.

[21] K. Miyachi and A Fukuda, 1998. *Antiferroelectric Liquid Crystals*, volume 2B of *Handbook of Liquid Crystals* edited by . D. Demus, J. Goodby, G.W. Gray, H.-W. Spiess, and V. Vill, Wiley VCH, pp. 665–691.

[22] K. Hori and K. Endo. Crystal structure and polymorphism of antiferroelectric mesogen, 4-[(S)-1-methylheptyloxycarbonyl]-phenyl-4'-octyloxybiphenyl-4-carboxylate (MHPOBC), 1993. Bull. Chem. Soc. Jpn., 66:46–50.

[23] Y. Ouchi, Y. Yoshioka, H. Ishii, K. Seki, N. Kitamura, M.and Noyori, Y. Takanishi, and I. Nishiyama. Effect of terminal branching structure of some liquid-crystalline biphenyl carboxylates on the stability of the antiferroelectric phase, 1995. J.Mater.Chem., 5:2297–2304.

[24] B. Jin, Z. Ling, Y. Takanishi, K. Ishikawa, H. Takezoe, A. Fukuda, M. Kakimoto, and T. Kitazume. Obliquely projecting chiral alkyl chains and their precession around the long core axes in the SmA phase of an antiferoelectric liquid crystal, 1996. Phys.Rev. E, 53:R4295–R4299.

[25] T. Nakai, H. Fujimori, D. Kuwahara, and S. Miyajima. Complete assignment of $^{13}$C-NMR spectra and determination of orientational order parameter for antiferroelectric liquid-crystalline MHPOBC, 1999. J. Phys. Chem. B, 103:417–425.

[26] E. Garcia, M.A. Glaser, N.A. Clark, and D.M. Walba. Hff: a force field for liquid cyrstal molecules, 1999. J. Mol. Struc., 464:39–48.

[27] B. Chen, M.G. Martin, and J.I. Siepmann. Thermodynamic properties of the Williams, OPLS-AA and MMFF94 all-atom force fields for normal alkanes, 1998. J.Phys.Chem.B, 102:2578–2586.

[28] M. J. Frisch, G. W. Trucks, H. B. Schlegela, P. M. W. Gill, B. G. Johnson, M. A. Robb, J. R. Cheeseman, T. Keith, G. A. Petersson, J. A. Montgomery, K. Raghavachari, M. A. Al-Laham, V. G. Zakrzewski, J. V. Ortiz, J. B. Foresman, Cioslowski, Stefanov J., B. B., A. Nanayakkara, Challacombe, M. C. Y. Peng, P. Y. Ayala, Wong Chen, W., Andres M. W., J. L., E. S. Replogle, R. Gomperts, R. L. Martin, D. J. Fox, J. S. Binkley, D. J. Defrees, J. Baker, J. P. Stewart, M. Head-Gordon, C. Gonzalez, and J. A. Pople. *Gaussian 94, Revision C.3*. Pittsburgh PA.

[29] B. Smith, S. Karaborni, and J.I. Siepmann. Computer simulations of vapor–liquid equilibria of n-alkanes, 1995. J. Chem. Phys., 102(5):2126–2139.

[30] W.L. Jorgensen, D.S. Maxwell, and J. Tirade-Rives. Development and testing of the OPLS all-atom force field on conformational energetics and properties of organic liquids, 1996. J. Am. Chem. Soc., 118:11225–11236.

[31] A.R. Leach. *Molelular Modelling*. Prentice Hall, 2001.

[32] W.D. Cornell, P. Cieplak, C.I. Bayly, and A. Kollman. Application of RESP

charges to calculate conformational energies, hydrogen bond energies, and free energies of solvation, 1993. J. Am. Chem. Soc., 115:9620–9631.

[33] Frank Schmauder. *Molekulardynamische Simulation smektischer chiraler Flssigkristallphasen.* PhD thesis, University of Dortmund, 2003. https://eldorado.uni-dortmund.de/handle/2003/2519.

[34] D. Paschek. MOSCITO, a molecular simulation package, v3.8, 1999. http://ganter.chemie.uni-dortmund.de/moscito.

[35] U. Essmann, L. Perera, M. L. Berkowitz, T. A. Darden, H. Lee, and L. G. Pedersen. A smooth Particle Mesh Ewald method, 1995. J. Chem. Phys., 103:8577.

[36] H.J.C Berendsen, J.P.M Postma, A DiNola, and W.F.v Gunsteren. Molecular dynamics with coupling to an external bath, 1984. J. Chem. Phys., 8(81):3684–3690.

[37] R. Bartolino, J. Doucet, and G. Durand. Molecular tilt in the smectic c phase: A zigzag model, 1978. Ann.Phys. (Paris), 3:389.

[38] Y. Takanishi, A. Ikeda, H. Takezoe, and A Fukuda. Higher smectic order parameters in liquid crystals determined by x-ray diffraction and the effect of antiferroelectricity, 1995. Phys. Rev. E, 51:400–406.

[39] K. Furukawa, K. Terashima, M. Ichihashi, S. Saitoh, K. Miyazawa, and T. Inukai. Chiral smectic C liquid crystals having an electronegative substituent ortho to the chrial tail group - a study of a factor determining the magnitude of spontaneous polarisation, 1988. Ferroelectrics, 85:451–459.

[40] H.R. Brand, P.E. Cladis, and H. Pleiner. Symmetry and defects in the $C_m$-phase of polymeric liquid crystals, 1992. Macromolecules, 25:7223–7226.

[41] J. Miyachi, J. Matsushima, Y. Takanishi, K. Ishikawa, Takezoe.H., and A. Fukuda. Spontaneous polarization parallel to the tilt plane in the antiferroelectric chiral SmC$_A$ phase of liquid crystals as observed by polarized infrared spectroscopy, 1995. Phys. Rev. B, 52:R2153–R2156.

[42] A.A. Muravski, F. Schmauder, A. Geiger, and A.A. Minko. Molecular theory of the ferroelectric and antiferroelectric phases in smectic liquid crystals. volume 5565 of *Proc. of SPIE*, pp. 135–140, 2004.

[43] A.D.L. Chandani, Y. Ouchi, Takezoe.H., A. Fukuda, K. Terashima, K. Furukawa, and A. Kishi. Novel phases exhibiting tristable switching, 1989. Jpn.J.Appl.Phys., 28:L1261–L1264.

# 6 Tables and Figures

| Simulation | T/K | $\frac{\rho}{\mathrm{g\,cm^{-3}}}$ | $d/\,\mathrm{nm}$ | $\tau_1$ | $\tau_2$ | $\tau_3$ | $\frac{\sqrt{<z^2>}}{d}$ | $t/\,\mathrm{ns}$ | cliniciy |
|---|---|---|---|---|---|---|---|---|---|
| SmX | 375K | 1.06 | 3.35 | 0.82 | 0.40 | 0.06 | 0.111 | 22.5 | syn |
| $\mathrm{SmC_A}$ | 375K | 1.06 | 3.59 | 0.75 | 0.28 | -0.03 | 0.132 | 37.5 | anti |
| $\mathrm{SmC_A}$ | 400K | 1.04 | 3.44 | 0.75 | 0.27 | -0.01 | 0.131 | 12.5 | anti |
| FSF | 375K | | 3.90 | | | | 0.130 | 8.0 | orthogonal |

Table 1: Overview of simulations performed. t: full length of simulation runs, including equilibration. The other data are averages over the last 2.5 ns, where the system is equilibrated. $\rho$: density. $d$: layer thickness. $\tau_i$: McMillan parameter (Eq. (5)). $\sqrt{<z^2>}$: width of center of mass distribution in the layer

CH3

chiral tail

core

achiral tail

(a) MHPOBC

$$\text{cry} \xrightarrow{357,2\,\text{K}} \text{SmC}_A \xrightarrow{391,6\,\text{K}} \text{SmC}_\gamma \xrightarrow{392,4\,\text{K}} \text{SmC} \xrightarrow{394,1\,\text{K}} \text{SmC}_\alpha \xrightarrow{395,2\,\text{K}} \text{SmA} \xrightarrow{421.2\,\text{K}} \text{iso}$$

(b) phase sequence of MHPOBC

O

X        O       Y

X = Ph, CH$_3$

Y = Ph, Ph–COOH,C(CH$_3$)$_2$

Ph     Ph

HO     Ph     Ph     COOH

(c) ester group in core

(d) biphenyl

O     Ph

O     Ph     Ph

O     Ph

CH$_3$

O

(e) achiral ether tail

(f) chiral ester tail
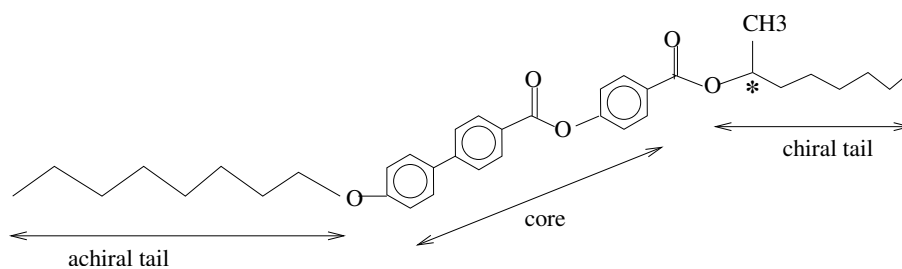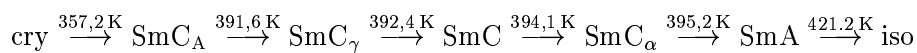
Figure 1: (a) Chemical structure of MHPOBC, (b) phase sequence of MHPOBC, (c-f) Fragments of MHPOBC which have been treated by ab-initio calculations to determine torsional potentials. In some cases we include 1,5-interactions as well as modifying the fragments. Torsions are indicated by arrows. [24, 43]
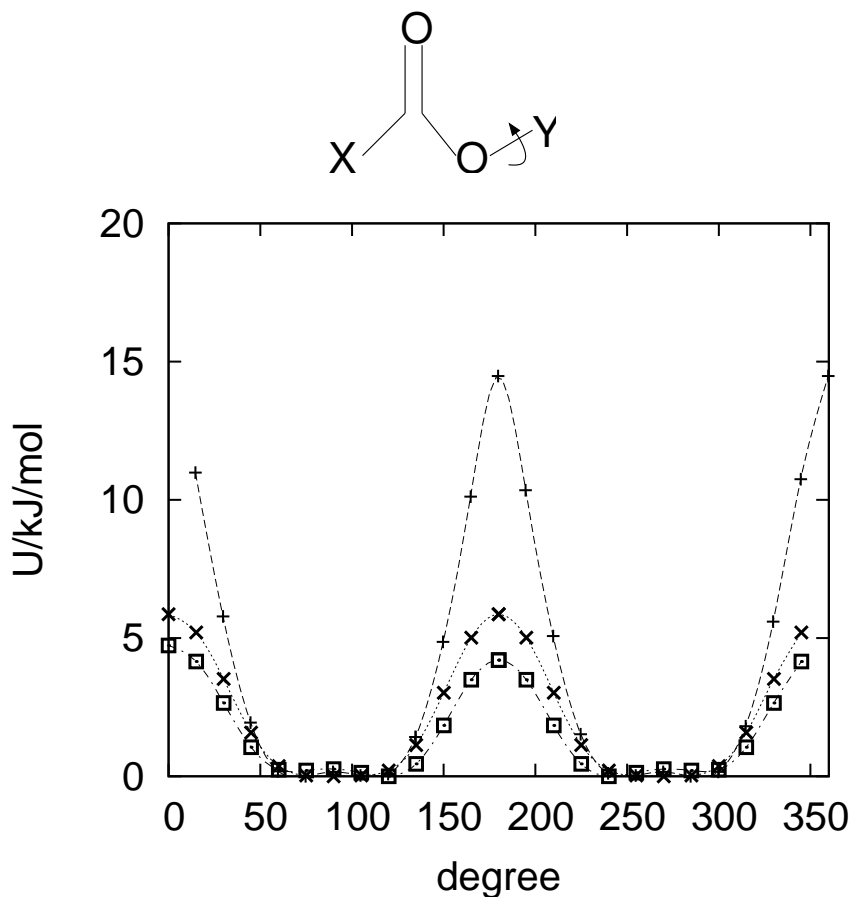
Figure 2: Change of the torsional potential with increasing extension of $\pi$- system. This potential determines the torsional flexibility in the core of MHPOBC. The torsional angle is marked by an arrow in the fragment. (pluses: $X = CH_3$, $Y = Ph$; crosses: $X = Y = Ph$; squares: $X = Ph$, $Y = Ph - COOH$) Symbols: from ab-initio calculations, lines: fits, using Eq.(1)
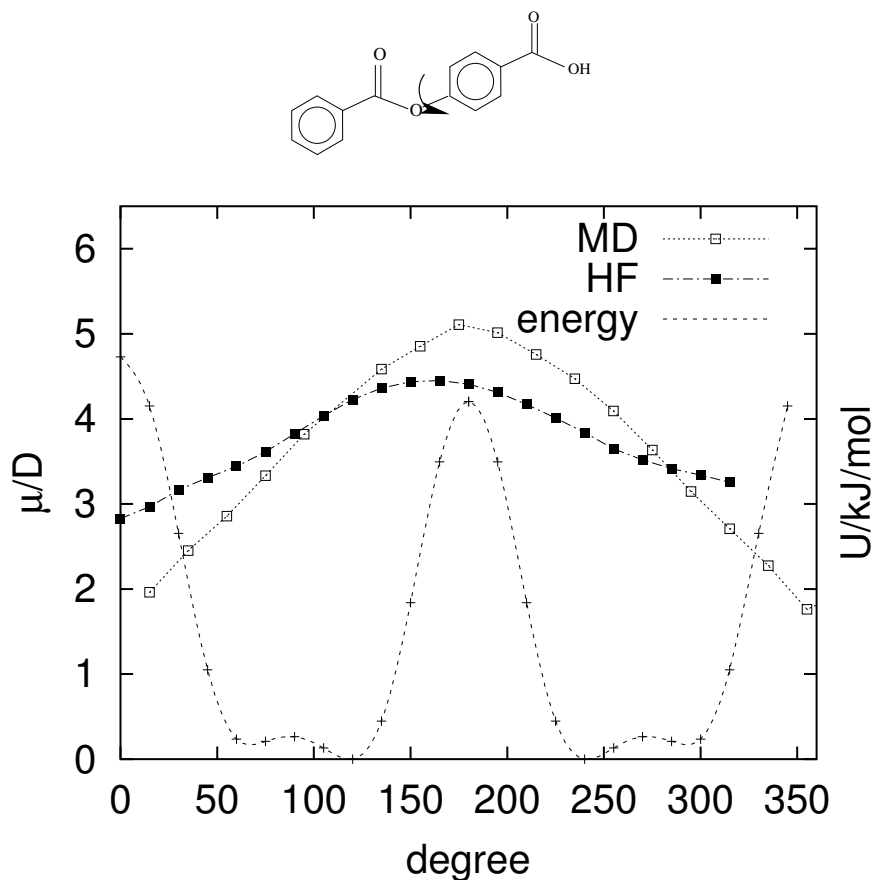
Figure 3: Change of molecular dipole moment of a fragment molecule with varying torsional angle. Values from ab-initio calculations (open squares) and from force field calculations (full squares) are shown. For comparison also the course of the minimized ab-initio energy at these torsion angles is given (short dashed line).
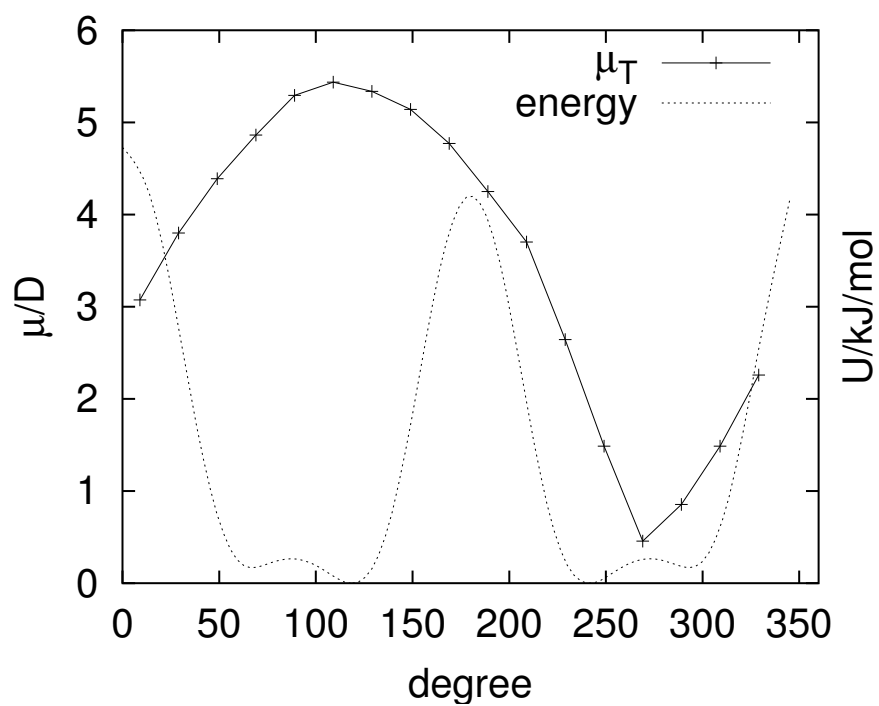
Figure 4: Change of molecular dipole moment of MHPOBC with varying torsional angle (dotted line: course of the torsion potential for rotation around the angle used in Fig. 2). The dipol moment is calculated from the partial charges of the force field used in the simulation.
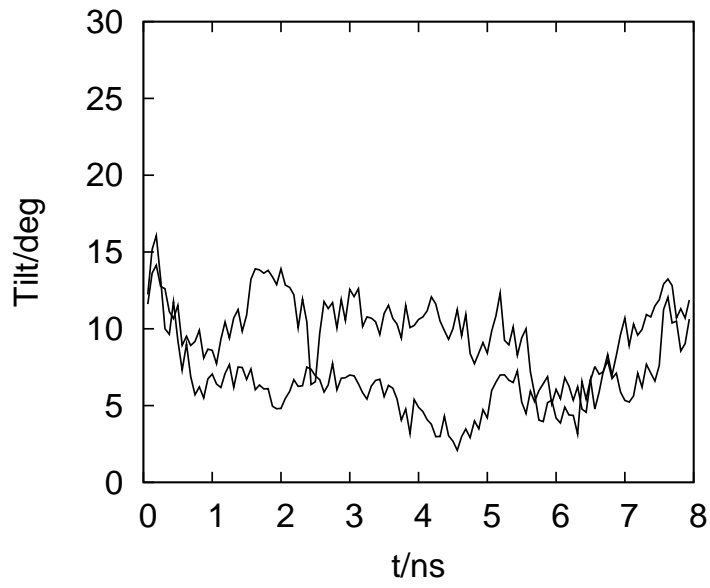
(a)
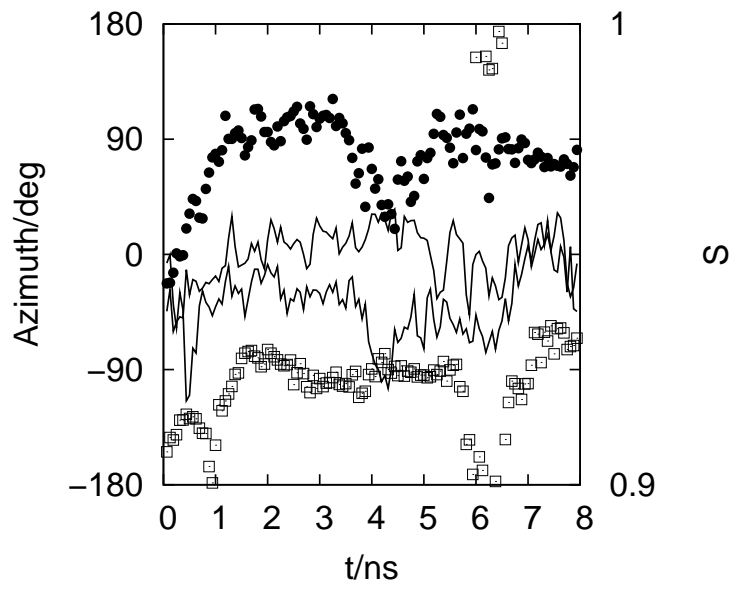


(b)

Figure 5: Characteristics of the FSF simulation run: (a) optical tilt in both layers, (b) order parameters S of both layers (lines) and azimuth angle of each layer (dots and squares)
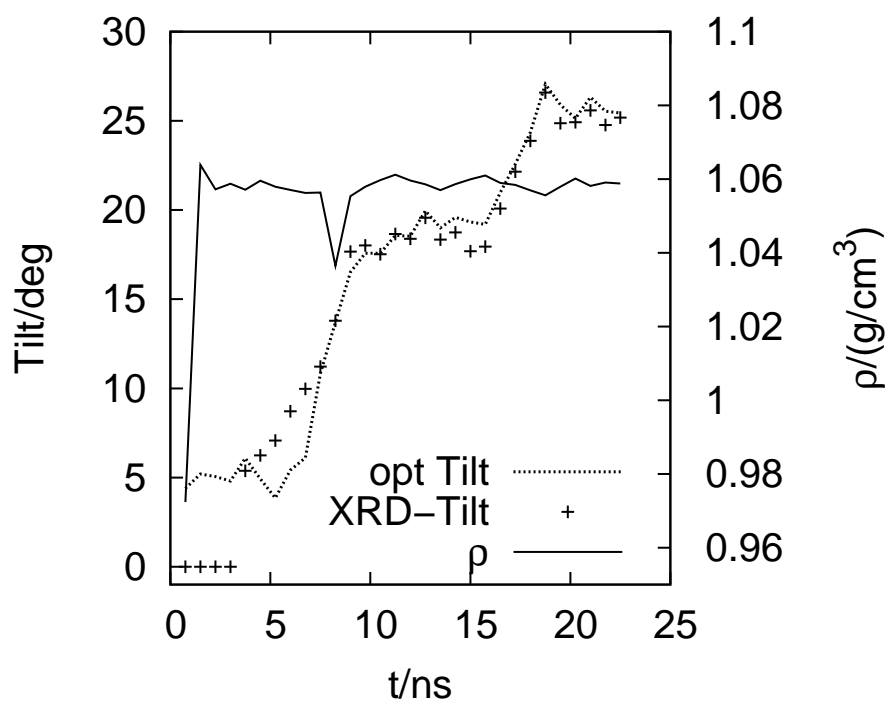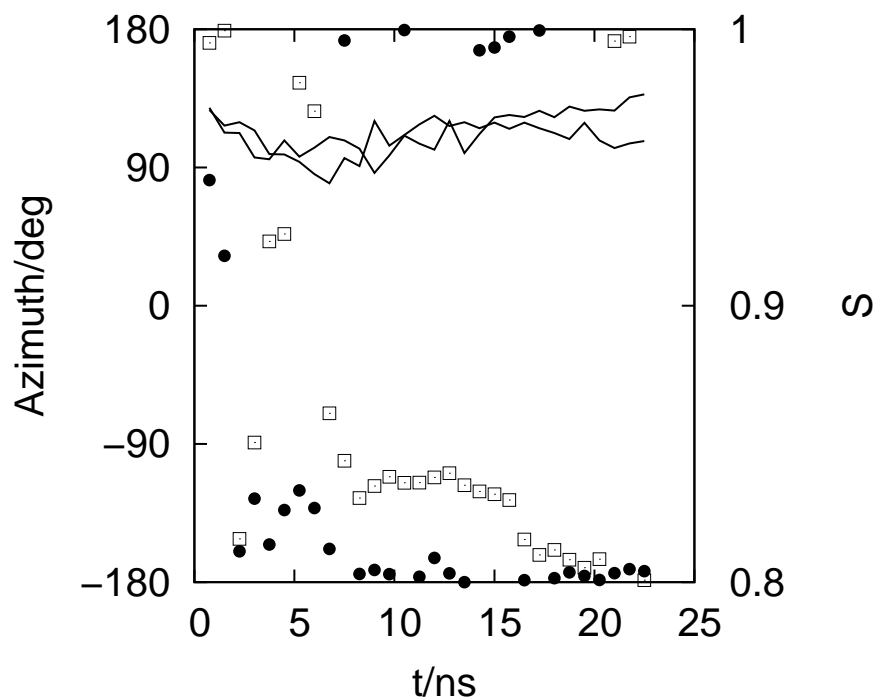
Figure 6: Characteristics of the SmX simulation run: (a) mass density $\rho$ (full line); optical tilt, averaged over both layers (dotted line); X-ray tilt (crosses); (b) order parameters S (full lines) and azimuth angles (dots and squares) for both layers.
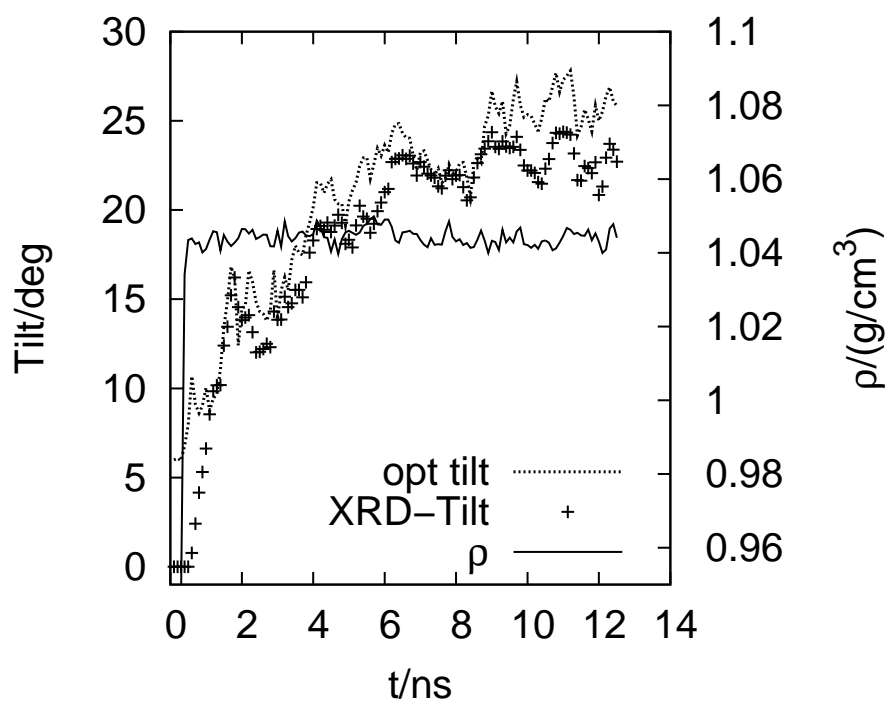
(a)
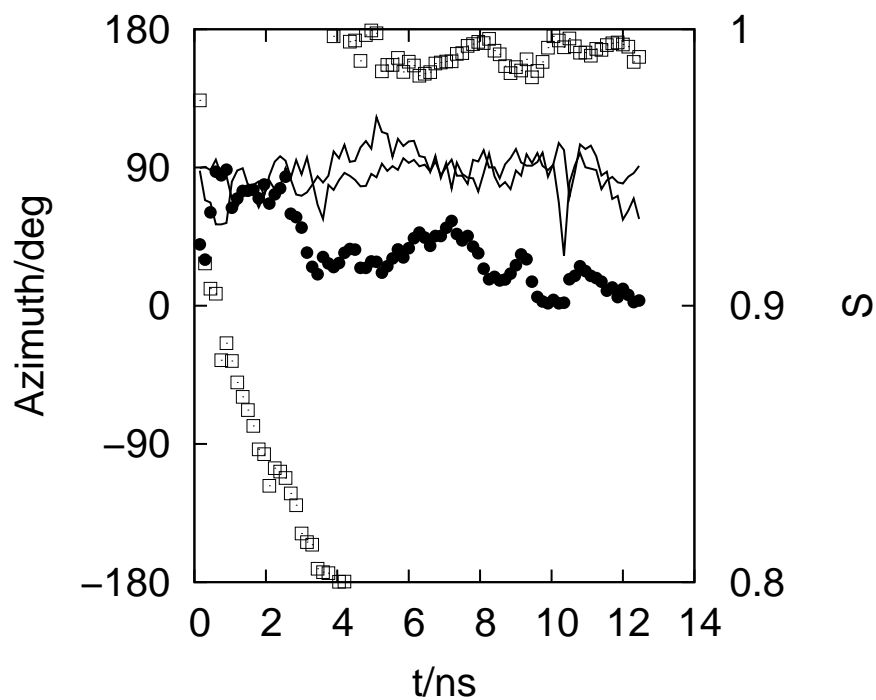


(b)

Figure 7: Characteristics of the SmC$_A$ simulation run at 400 K: (a) mass density (full line), optical (dotted line) and X-ray tilt (crosses, averaged over both layers) (b) order parameters S of both layers (full lines) and azimuth angle of each layer (dots and squares).
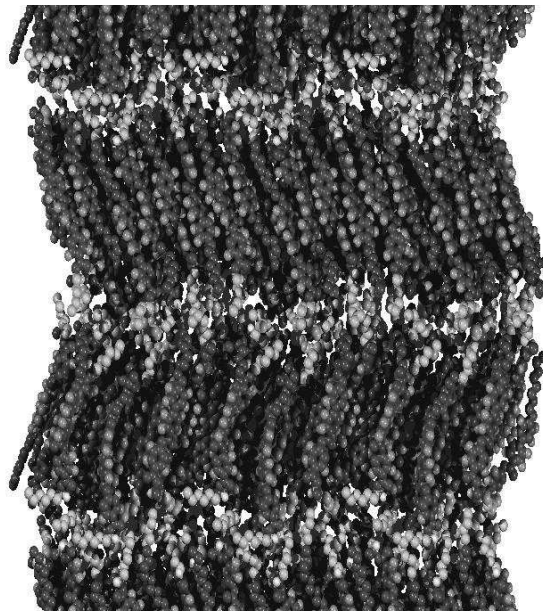
(a) SmC$_A$
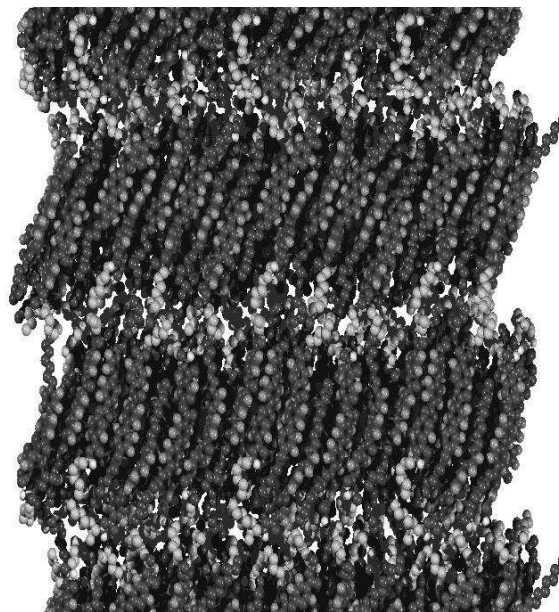


(b) SmX

Figure 8: Snapshot from Simulations SmC$_A$(400K) and SmX(375K). Anticlinic and syn-clinic orientations are clearly seen. Each picture comprises severeal periodic images of the simulation box to show the structures more clearly.
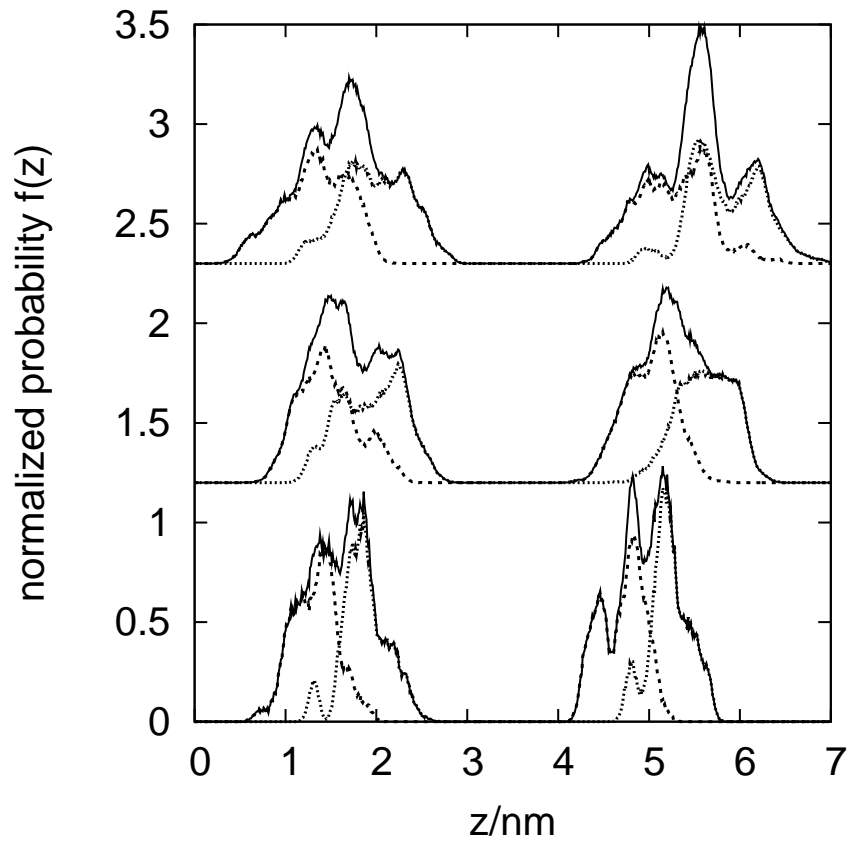
Figure 9: Center of mass distribution along the layer normal. From top to bottom: FSF, SmC$_A$, SmX (all at 375 K). Each simulation is subdivided into contributions from molecules directed in $+z$-direction (dotted) and $-z$-direction (dashed dotted). The overall distribution is also shown (full line).
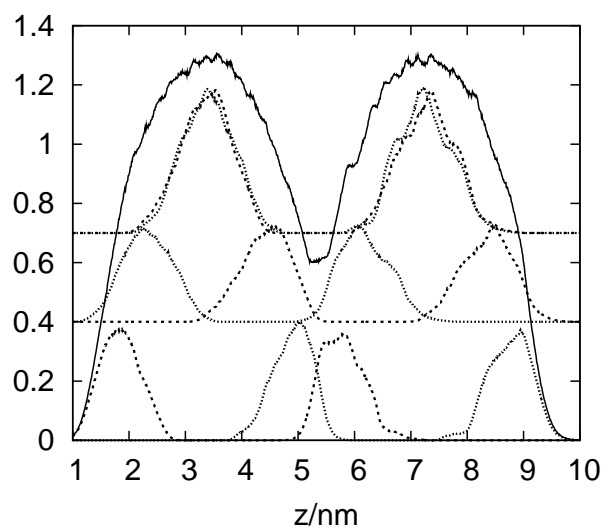
(a) FSF
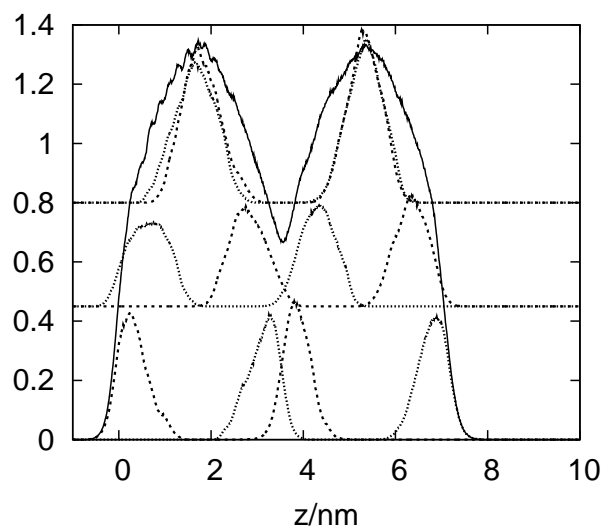


(b) SmC$_A$

Figure 10: Subdivision of the mass density profile $\rho(z)$ (full line) in the FSF-simulation (a) and in the SmC$_A$ simulation at $375\,K$ (b) into contribution of the chiral tails, achiral tails and biphenyl group (shifted from bottom to top for clarity). The dotted and dashed-dotted distributions on the same level represent groups in oppositely oriented MHPOBC molecules (Each atom enters as individual mass center into these distributions).
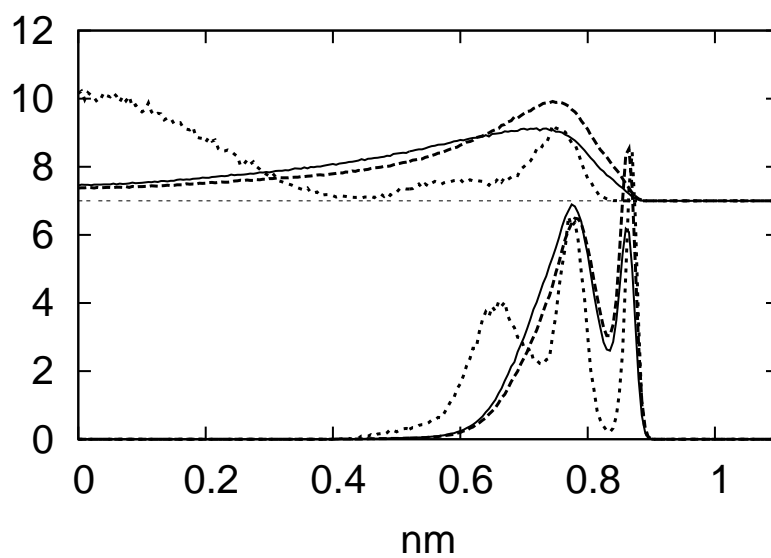
(a) chiral tail
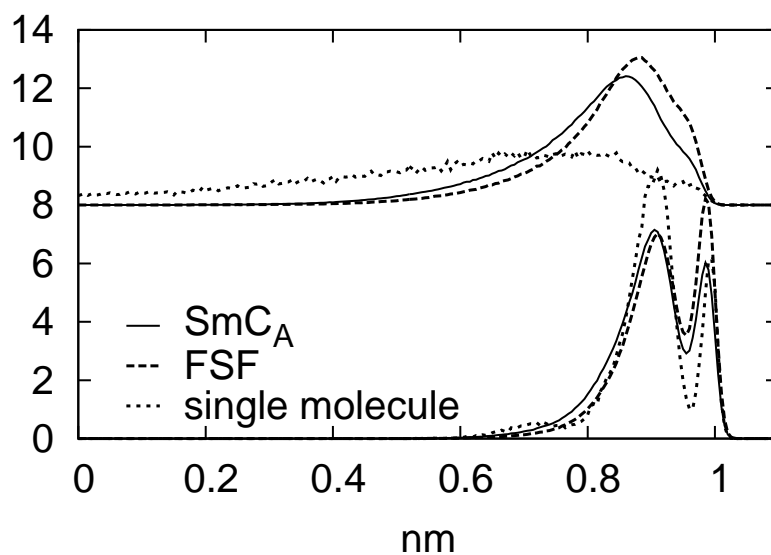


(b) achiral tail

Figure 11: Conformational distributions of chiral (a) and achiral tail (b) Shown are the length distributions of the projections of the tail vectors (see text) to the core vector direction (shifted up) and the end-to-end distance distributions of the absolute (non projected) lengths of the tail vectors (bottom).
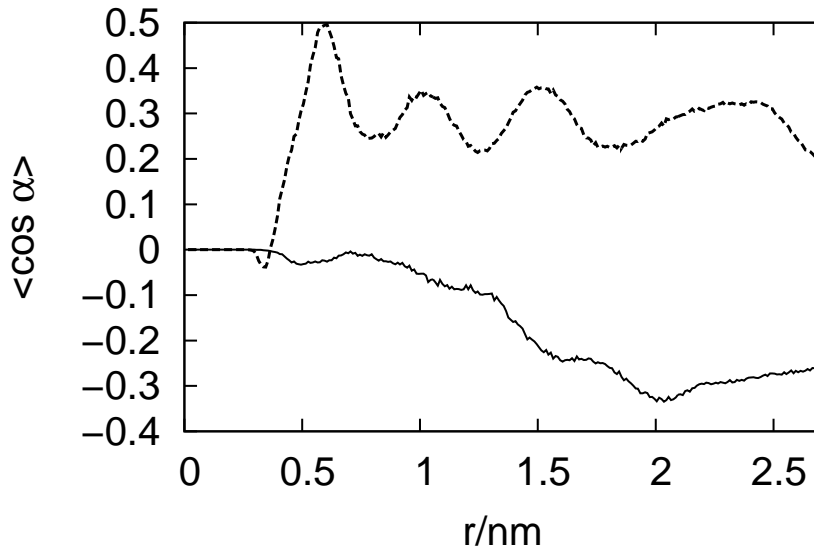
(a) SmX
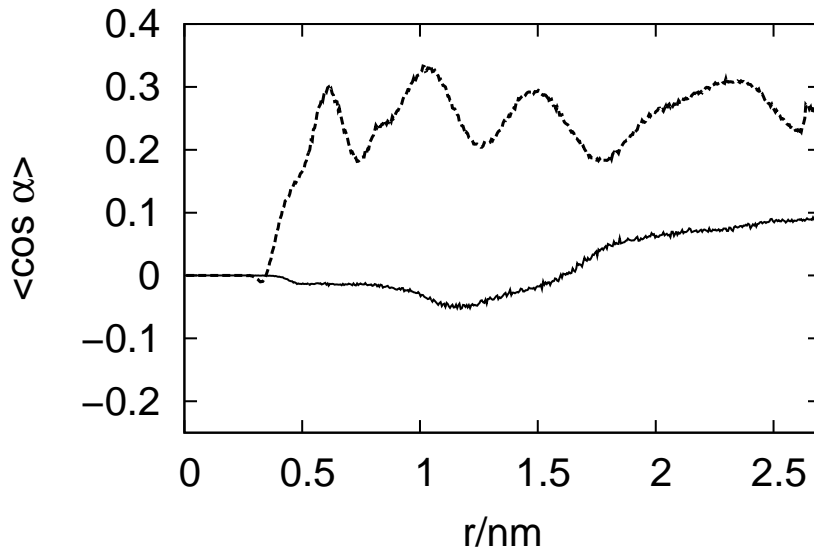


(b) SmC$_A$

Figure 12: Inter- and intralayer orientational correlation functions of the carbonyl groups $g_1^{CO}(\mathbf{r})$ (full and dashed lines respectively) in the synclinic SmX (a) and anticlinic SmC$_A$ (b) structures at 375K. The interlayer functions are calculated for pairs of antiparallel molecular core orientation, the intralayer functions for parallely oriented molecules (see text).
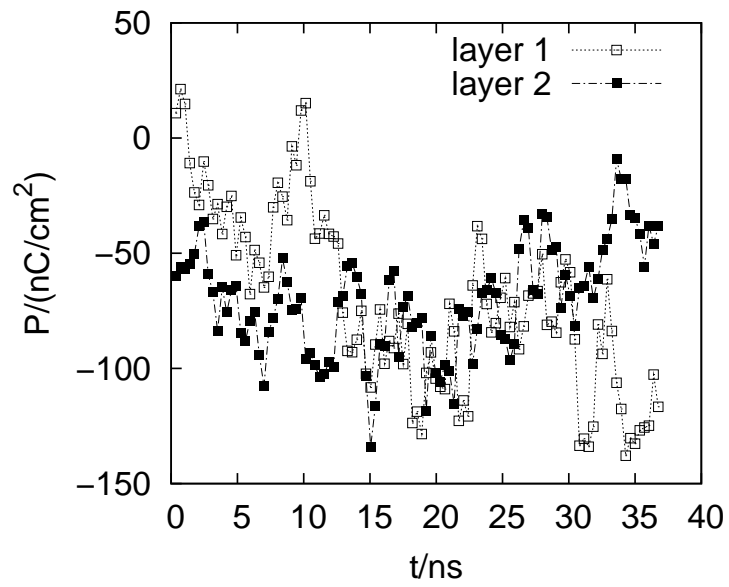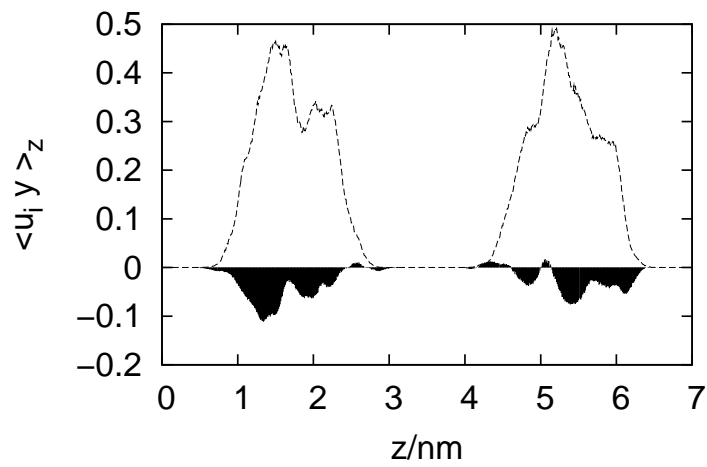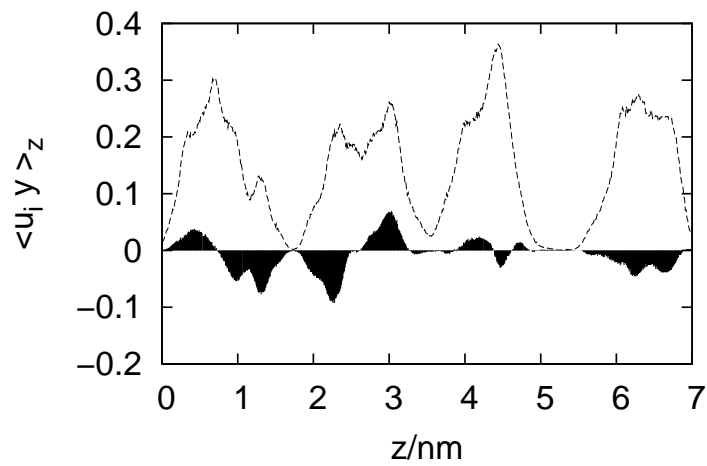
Figure 13: Development of spontaneous polarization $P_s$ in the two layers of simulation SmC$_A$ at 375 K. Due to the opposite tilt in the two layers, the polarisation vector also point in opposite direction (see text).
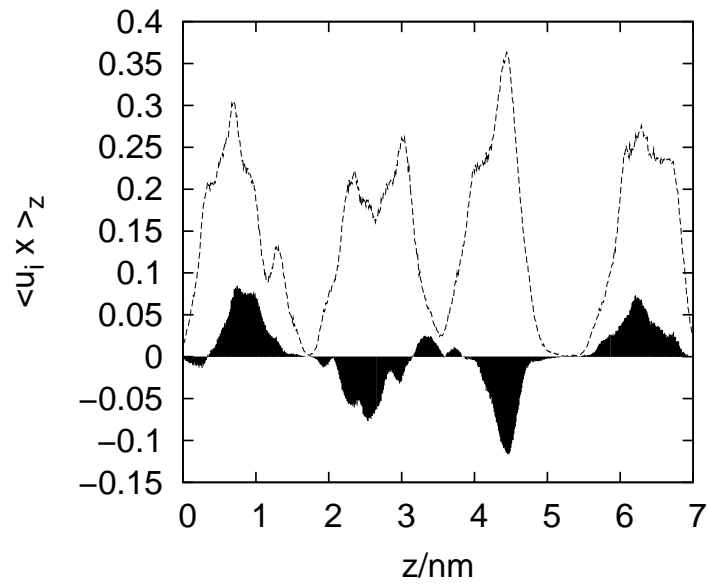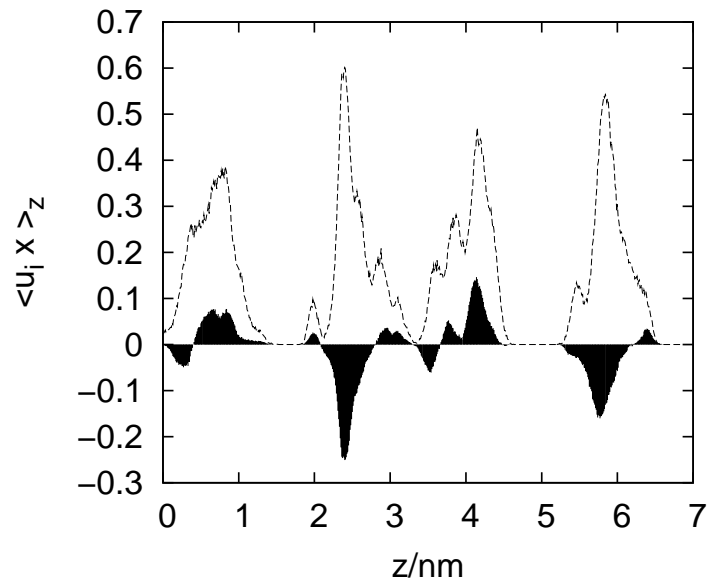
(a) core



(b) tail

Figure 14: Polarisation distribution $< \mathbf{u}_i \cdot \mathbf{y} >_z$ (black area) of core (a) and lateral (b) carbonyl groups in the simulation $SmC_A$ at 375 K. Dashed line: The number density profiles of core (a) and of lateral carbonyl carbons (b). The core carbonyl C-atom is close to the center of mass, the lateral carbonyl C-atom close to the chiral center.

(a) SmC$_A$,anticlinic



(b) SmX, synclinic

Figure 15: Number density profile of lateral carbonyl carbons (dashed line, arbitrary units) and related $P_x$ profile (black area, see text). Results are shown for simulation SmC$_A$ at 375 K (a) and SmX (375K) (b).
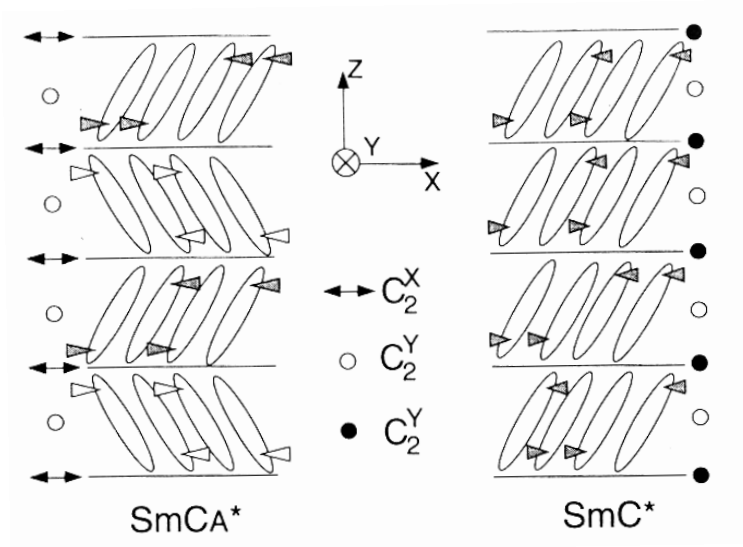
Figure 16: In-plane spontaneous polarisation in the $SmC_A$ and SmX simulations produced by the lateral CO groups. Also shown are the orientation and position of the different $C_2$ symmetry axes (drawn after Fig.10 of [21]). The orientation of different axes are marked by by the symbols given in the central colums. The horizontal triangels represent the local dipole moments.